

## PAPER

[View Article Online](#)  
[View Journal](#) | [View Issue](#)Cite this: *Nanoscale Adv.*, 2020, 2, 4220Enhancement of the photocatalytic synchronous removal of Cr(VI) and RhB over RP-modified flower-like SnS<sub>2</sub>†Xue Bai,<sup>‡ab</sup> Yanyan Du,<sup>‡a</sup> Wenhua Xue,<sup>a</sup> Xiaoyun Hu,<sup>©c</sup> Jun Fan,<sup>©a</sup> Jianli Li<sup>©b</sup> and Enzhou Liu<sup>©\*a</sup>

Although photocatalysis is frequently employed to remove various pollutants in water, it still suffers from low efficiency due to the rapid recombination of photogenerated electrons and holes. In this study, a red phosphorus/tin disulfide (RP/SnS<sub>2</sub>) composite photocatalyst is fabricated by loading nano-sized RP on flower-like SnS<sub>2</sub> films with a facile hydrothermal method. It is noteworthy that the 2D heterojunction formed between SnS<sub>2</sub> and RP provided channels for the rapid transfer of photon-generated carriers and their effective separation. Furthermore, the separated electrons can react with absorbed O<sub>2</sub> for the generation of superoxide radicals (<sup>•</sup>O<sub>2</sub><sup>−</sup>), thereby impacting the photocatalytic degradation oxidation reaction. The application of photocatalytic synchronous removal of Cr(VI) and RhB over RP/SnS<sub>2</sub> was implemented first. Compared with pristine SnS<sub>2</sub>, the photocatalytic degradation activity of Cr(VI) and RhB over the RP/SnS<sub>2</sub> composite was significantly enhanced and the kinetic rate constant reached 8.2, which is 10.8 times that of pristine SnS<sub>2</sub>. Moreover, the hybrid photocatalysts exhibited prominent reusability and stability. Therefore, a photocatalytic degradation mechanism and pathway of carriers are proposed in the study. Furthermore, it is considered that the present study is a promising method in the treatment of wastewater by photocatalysis.

Received 15th June 2020

Accepted 28th July 2020

DOI: 10.1039/d0na00489h

[rsc.li/nanoscale-advances](http://rsc.li/nanoscale-advances)

## 1. Introduction

Currently, various semiconductors as photocatalysts, characterized by low cost, minimum efficiency, less stability and low toxicity are investigated extensively for water treatment.<sup>1–5</sup> Under sufficient light energy, electrons and holes are generated and transferred to undergo oxidation–reduction reactions on the surfaces of photocatalytic materials.<sup>6</sup> Consequently, the energy band gap ( $E_g$ ) and position of the conduction band (CB) and valence band (VB) critically impact this process. Given the diversity of contaminants in their surroundings and production, photocatalysts are specifically designed for multiple reactions.<sup>7,8</sup> Thus, the photocatalytic activity is dependent on the REDOX potential of semiconductors. Furthermore, rapid separation and migration capabilities result in photocatalytic performance with higher efficiency.<sup>9–13</sup> Accordingly, nano-sized semiconductors, especially the two-dimensional (2D) materials

have been recognized as one of the most promising strategies to synthesize catalysts in a conducive environment exhibiting high efficiency.<sup>14–17</sup>

Tin disulfide (SnS<sub>2</sub>) is a metal sulfide photocatalyst with response to visible light and band gap of 2.0–2.25 eV.<sup>18,19</sup> It also exhibits good stability in various aqueous solutions, making it a promising photocatalyst for pollutant degradation.<sup>20–26</sup> The practical performance of SnS<sub>2</sub> materials is associated with crystallinity, morphology, size, *etc.* Intensive research has been performed to regulate the morphology of SnS<sub>2</sub>, and various nanostructures were successfully built over the past few years.<sup>27–29</sup> In general, photocatalysts with large visible-light absorbance do not guarantee photocatalytic efficiency. The development of high performance SnS<sub>2</sub>-based photocatalysts remains vital for the application of photocatalysis on large scale (Table S1†). Red phosphorus (RP) is an earth abundant element that exhibits high photocatalytic activity with narrow band gap in the range of 1.4–2.0 eV (ref. 30) and prevails over most of the traditional metal-based photocatalysts with its good visible light response.<sup>31</sup> Fortunately, SnS<sub>2</sub> and RP have matched band potentials with both CB and VB potentials of RP being more negative than those of SnS<sub>2</sub>, and thereby, thermodynamically allowing the photogenerated electron transfer from the CB of RP to the CB of SnS<sub>2</sub> under visible light irradiation. Moreover, the reverse transmission of holes occurs from the VB of SnS<sub>2</sub> to the VB of RP. Promoted by the photogenerated separation of

<sup>a</sup>School of Chemical Engineering, Northwest University, Xi'an 710069, P. R. China. E-mail: liuenzhou@mwu.edu.cn

<sup>b</sup>Chemistry and Material Science College, Northwest University, Xi'an, 710127, P. R. China. E-mail: lijianli@mwu.edu.cn

<sup>c</sup>School of Physics, Northwest University, Xi'an 710069, P. R. China

† Electronic supplementary information (ESI) available. See DOI: 10.1039/d0na00489h

‡ Xue Bai and Yanyan Du contributed equally to the present study.

electrons and holes in  $\text{SnS}_2$ , more efficient photocatalytic reaction can be achieved. It is noteworthy that the 2D/2D heterostructure between  $\text{SnS}_2$  and RP shortens the transmission path, thereby accelerating carrier transportation and limiting the recombination process.

In this study, the synthesis of RP-modified flower-like  $\text{SnS}_2$  for the synchronous removal of  $\text{Cr}(\text{vi})$  and RhB is reported. The uniform dispersible 2D structure was built by a facile hydrothermal method, resulting in effective charge separation and significantly enhanced photocatalytic activity. Moreover, the quick  $\text{e}^-$  transfer significantly inhibited the electron-hole pair recombination and facilitated the release of photocatalytic active groups ( $\text{O}_2^-$ ). The photocatalytic activity of  $\text{SnS}_2$  is significantly enhanced by the presence of RP. The  $K_{\text{app}}$  of the RP/ $\text{SnS}_2$  composite for the removal of  $\text{Cr}(\text{vi})$  and RhB is 8.2 and 10.8 times higher than the degradation kinetic constant of pure  $\text{SnS}_2$ , as well as 8.6 and 15.7 times higher than that of pure RP. Overall, the prominent photocatalytic efficiency and stability of the simultaneous removal of  $\text{Cr}(\text{vi})$  and RhB with the RP/ $\text{SnS}_2$  composite makes a significant step toward the application of photocatalysis in actual water treatment.

## 2. Materials and methods

### 2.1 The preparation of RP-modified flower-like $\text{SnS}_2$ hybrid

All chemicals were of analytical grade and employed without further purification. Moreover, the RP-modified flower-like  $\text{SnS}_2$  was generated following the 3 steps below:

(1) The commercial RP was milled with water and sieved to remove the coarse part. Subsequently, the hydrothermal treatment was conducted at  $200^\circ\text{C}$  for 12 h, the RP was washed, and centrifugal separation with deionized water was performed repeatedly to produce nanostructured RP for subsequent use.

(2) Then, 2 mmol  $\text{SnCl}_4 \cdot 5\text{H}_2\text{O}$  and 5 mmol  $\text{CH}_3\text{CSNH}_2$  (thioacetamide) were adequately dissolved in 60 mL of ethanol to generate a transparent solution. Different amounts of the nanostructured RP (*i.e.* 80 mg, 137 mg, 213 mg, 320 mg and 480 mg) were dispersed in the transparent solution, stirred for 30 min to mix well, then ultrasonic treatment was performed for 2 h.

(3) The suspension was transferred to a high-pressure reactor and heated at  $180^\circ\text{C}$  for 12 h. After being cooled down to ambient temperature, the samples were harvested by

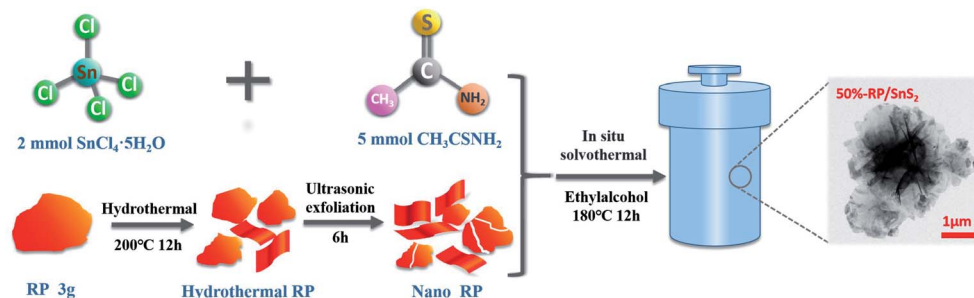
centrifugation, washed with deionized water several times, and then dried at  $60^\circ\text{C}$  with a drying oven. The obtained samples were respectively labeled as 20%-RP/ $\text{SnS}_2$ , 30%-RP/ $\text{SnS}_2$ , 40%-RP/ $\text{SnS}_2$ , 50%-RP/ $\text{SnS}_2$  and 60%-RP/ $\text{SnS}_2$ . The specific preparation processes of the samples are illustrated in Scheme 1.

### 2.2 Characterization

The crystalline phases were characterized by a Shimadzu XRD-6000 powder diffractometer. Under a scanning electron microscope (SEM, Carl Zeiss SIGMA) and a transmission electron microscope (TEM, Tecnai G2 F20S-TWIN), the morphology and microstructure of photocatalysts were identified. X-ray photoelectron spectroscopy (XPS) was performed with a Kratos AXIS NOVA spectrometer. UV-vis diffuse reflectance spectra were collected on a Shimadzu UV-3600 UV/vis/NIR spectrophotometer. Photoluminescence (PL) spectra were obtained on a fluorescence spectrophotometer (Hitachi F-7000). With a three-electrode system (CHI-660E, Chenhua Instruments Co., Shanghai, China), the photoelectrochemical experiments were performed. A Pt wire and saturated calomel electrode (SCE) acted as counter electrode and reference electrode, respectively. The catalyst powder was deposited on a fluoride tin oxide (FTO) substrate to serve as the working electrode. A 0.5 M  $\text{Na}_2\text{SO}_4$  aqueous solution acted as the electrolyte. A 300 W xenon lamp (MICROSOLAR300UV, Beijing Perfect light) equipped with a 420 nm cutoff filter ( $k > 420$  nm) was employed as a visible light source.

### 2.3 Photocatalytic activity evaluation

The photocatalytic activity of the as-synthesized  $x$ -RP/ $\text{SnS}_2$  ( $x = 20, 30, 40, 50$  and  $60$ ) was examined by the simultaneous removal of  $\text{Cr}(\text{vi})$  ( $\text{K}_2\text{Cr}_2\text{O}_7$  as the source of  $\text{Cr}(\text{vi})$ ) and RhB. A Xe lamp (300 W) was used as the irradiation source. Approximately 35 mg of photocatalyst was dispersed in the 100 mL of solution containing  $\text{Cr}(\text{vi})$  ions (40 ppm) and RhB (10 ppm). Prior to irradiation, the suspension was stirred in the dark for 30 min to reach the adsorption-desorption equilibrium, after which the process went on for 50 min under light irradiation. 3.5 mL of the solution was harvested and subsequently centrifuged at 10 000 rpm to separate the photocatalyst. The clear solution was used to determine the content of  $\text{Cr}(\text{vi})$  and RhB by UV-vis spectroscopy, and the absorbance maximum ( $\lambda_{\text{max}}$ ) of  $\text{Cr}(\text{vi})$  and RhB was at 356 nm and 554 nm, respectively.



Scheme 1 Schematic illustration of the preparation of RP/ $\text{SnS}_2$ .



### 3. Results and discussion

#### 3.1 Structural characterization and photocatalytic activity evaluation

Fig. 1 presents the typical X-ray diffraction (XRD) patterns of the as-fabricated samples. The pattern of RP features one distinct peak at  $15.19^\circ$ , which corresponds to the (102) plane of the amorphous RP. For the  $\text{SnS}_2$  sample, all the peaks can be readily indexed to hexagonal  $\text{SnS}_2$  (JCPDS 01-1010), in which peaks at  $15.0^\circ$ ,  $28.3^\circ$ ,  $32.1^\circ$ ,  $42.2^\circ$ ,  $50.1^\circ$  and  $52.551^\circ$  correspond to the (001), (100), (101), (102), (110) and (111) planes, respectively. No difference is identified in the diffraction peaks of  $\text{SnS}_2$  before and after hydrothermal treatment with RP (Fig. 1(a)). However, the position of the sample peak at  $15.0^\circ$  shifts from the pure  $\text{SnS}_2$  sample position to a lower degree, according to Fig. 1(b), which is probably caused by the formation of a heterojunction between RP and  $\text{SnS}_2$  and the lattice deformation of  $\text{SnS}_2$ .<sup>32</sup>

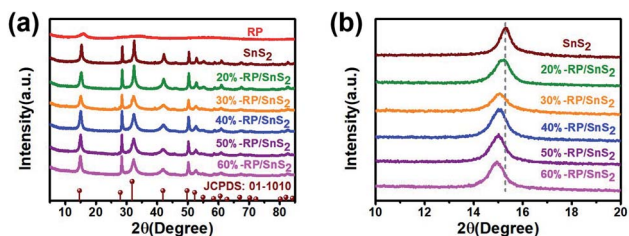


Fig. 1 XRD patterns of (a) full spectra and (b) magnified spectra of samples RP,  $\text{SnS}_2$ , and  $x\text{-RP/SnS}_2$ .

Besides, the  $x\text{-RP/SnS}_2$  structural transition can be attributed to the introduction of RP in the  $\text{SnS}_2$  layered structure (Fig. 3).

To assess the photocatalytic activities, the as-prepared samples were applied for the simultaneous photocatalytic removal of  $\text{Cr(VI)}$  and RhB. Fig. 2 illustrates the removal rate–time relationship of the samples during 30 min of stirring in the dark and 50 min illumination, in which only 8.0% and 1.9% of  $\text{Cr(VI)}$  and RhB remained after 50 min over 50%-RP/ $\text{SnS}_2$ . However, pure  $\text{SnS}_2$  and RP exhibited relatively weak capability toward the reduction of  $\text{Cr(VI)}$  and the decolorization of RhB; the residual amounts were nearly 50.2% and 18.5% for  $\text{SnS}_2$ , and 88% and 65.3% for RP, respectively. Fig. S1† presents the reduction of  $\text{Cr(VI)}$  (with UV absorption peak at 554 nm) and decolorization of RhB (with UV absorption peak at 354 nm) by 50%-RP/ $\text{SnS}_2$ ,  $\text{SnS}_2$  and RP. As expected, the modification of  $\text{SnS}_2$  by RP improved the photocatalytic reduction of  $\text{Cr(VI)}$  and oxidation of RhB simultaneously. Besides, the reactions were identified to be in accordance with  $-\ln(C/C_0) = K_{\text{app}}t$  (first-order kinetic equation), where  $K_{\text{app}}$  denotes the kinetic rate constant,  $C_0$  represents the original concentration of solution,  $t$  indicates the reaction time and  $C$  is the solution concentration at reaction time  $t$ . Fig. 2(c) suggests that the slope value of the fitting lines are  $0.04494 \text{ min}^{-1}$  and  $0.06692 \text{ min}^{-1}$ , equated with the  $K_{\text{app}}$  of the 50%-RP/ $\text{SnS}_2$  composite for the removal of  $\text{Cr(VI)}$  and RhB, exhibiting 8.2 and 10.8 times higher degradation kinetic constants than that of pure  $\text{SnS}_2$  (as shown in Fig. S4(a)†) and 8.6 and 15.7 times higher than that of pure RP (as shown in Fig. S4(b)†). Moreover, by cycling the photocatalytic experiments, the performance stability and reusability of 50%-RP/ $\text{SnS}_2$  photocatalysts were investigated. As revealed from the

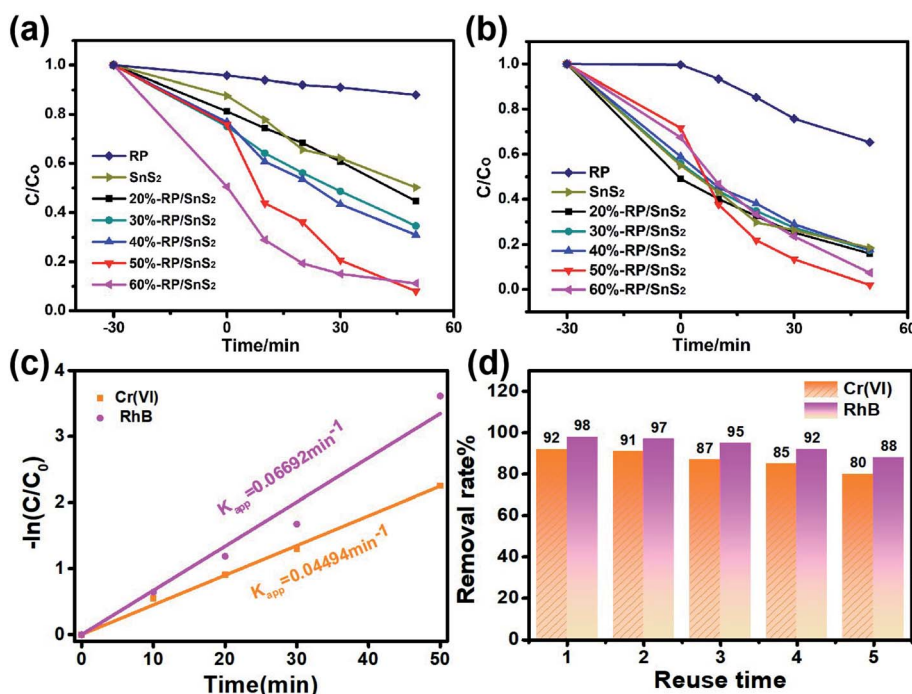


Fig. 2 Comparison of the effect of photocatalytic simultaneous removal of (a)  $\text{Cr(VI)}$  and (b) RhB by RP,  $\text{SnS}_2$ , and  $x\text{-RP/SnS}_2$ . (c) the fitted reaction kinetic curves ( $-\ln(C/C_0) = kt$ ) and (d) recycling test runs for five times in the photocatalytic removal of  $\text{Cr(VI)}$  and RhB by 50%-RP/ $\text{SnS}_2$ .





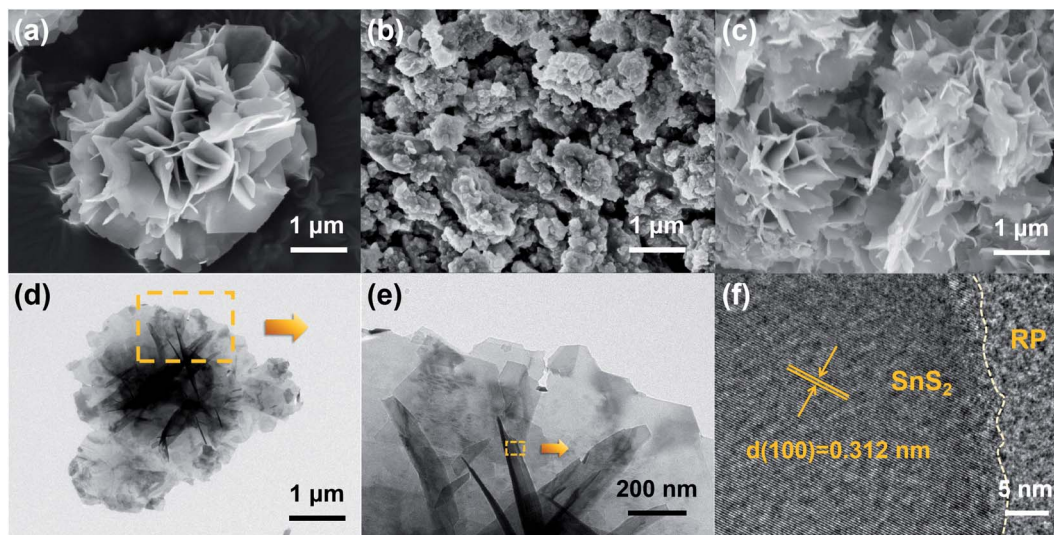


Fig. 3 SEM images of (a)  $\text{SnS}_2$ , (b) RP, (c) 50%-RP/ $\text{SnS}_2$ , (d and e) TEM and (f) HRTEM images of 50%-RP/ $\text{SnS}_2$ .

results of the recycling degradation experiments of Cr(vi) and RhB simultaneously in Fig. 2(d), there was a minor decrease after five cycles. Overall, 50%-RP/ $\text{SnS}_2$  exhibited a relatively optimal and comprehensive performance. Thus, the analyses of the other samples are not presented in the following discussion.

The surface and interface characteristics of the composite significantly enhanced the photocatalytic efficiency. SEM and TEM images were examined for the interfacial state and morphological structure of RP-modified flower-like  $\text{SnS}_2$ . As revealed from Fig. 3(a) and (b), the prepared  $\text{SnS}_2$  and RP exhibited nano-sized sheets with flower and fragment structures, respectively. The morphology of 50%-RP/ $\text{SnS}_2$  presented in Fig. 3(c) indicated that the fragments were uniformly scattered on the planes. In this nanocomposite, RP nanosheets act as a support to amplify the inner space of the  $\text{SnS}_2$  nanostructure, which may provide more transmission channels for carriers. The elemental mapping images of P, S and Sn in-plane and the EDS spectrum of 50%-RP/ $\text{SnS}_2$  (Fig. S2†) also confirmed the uniform dispersibility of RP on  $\text{SnS}_2$ . TEM and HRTEM images (Fig. 3(d)–(f)) further showed the morphological structure between  $\text{SnS}_2$  and RP, exhibiting effective contact and close interfaces, in which the lattice fringes of the sample with a  $d$  spacing of 0.312 nm can be assigned to the (100) lattice planes of  $\text{SnS}_2$ . Obviously, the RP modification strategy did not modify the flower-like structure of  $\text{SnS}_2$ . The construction of a 2D heterojunction between RP and  $\text{SnS}_2$  may reduce the resistance and speed up the transmission of charge carriers, which was verified by the electrochemical characterizations, as shown in Fig. 7. Furthermore,  $\text{N}_2$  sorption was measured to determine the specific surface area ( $S_{\text{BET}}$ ) and corresponding pore structure (Fig. 4). Moreover, the  $S_{\text{BET}}$  of  $\text{SnS}_2$ , RP and 50%-RP/ $\text{SnS}_2$  samples was determined as 35.38, 36.79 and 40.96  $\text{m}^2 \text{g}^{-1}$ , respectively (Table 1). Minor variations were identified in the  $S_{\text{BET}}$  and pore volume of the 50%-RP/ $\text{SnS}_2$  compared with  $\text{SnS}_2$ , suggesting that the composite does not generate agglomeration and has good dispersibility. It is noteworthy that

the pathway between them might lead to an efficient charge transfer.

### 3.2 X-ray photoelectron spectroscopy (XPS)

X-ray photoelectron spectroscopy (XPS) was performed to delve into the chemical composition and analyze the chemical states of 50%-RP/ $\text{SnS}_2$ . Fig. 5(a) presents the full survey spectrum, suggesting that the elements the composites contained complied with the chemical composition of the photocatalyst. The high-resolution P 2p spectrum of RP illustrated in Fig. 5(b) displays two main peaks at 130.3 eV and 131.4 eV, assigned to P 2p<sub>3/2</sub> and 2p<sub>1/2</sub>, respectively. The corresponding peak positions of RP/ $\text{SnS}_2$  shift to 130.6 and 133.1 eV. The Sn 3d spectrum of

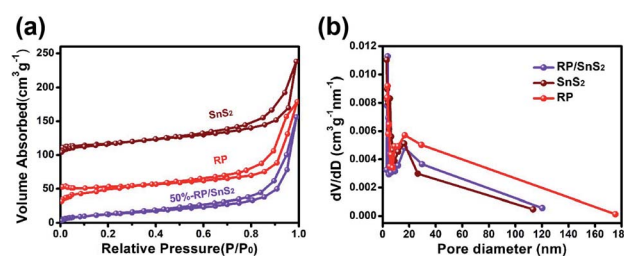


Fig. 4 (a)  $\text{N}_2$  adsorption–desorption isotherms and (b) the pore size distribution of  $\text{SnS}_2$ , RP and 50%-RP/ $\text{SnS}_2$  samples.

Table 1  $S_{\text{BET}}$ , pore diameter and pore volume of  $\text{SnS}_2$ , RP and 50%-RP/ $\text{SnS}_2$  samples

Samples	$S_{\text{BET}}$ ( $\text{m}^2 \text{g}^{-1}$ )	Pore diameter (nm)	Pore volume ( $\text{cm}^3 \text{g}^{-1}$ )
$\text{SnS}_2$	35.38	3.05	0.20
RP	36.79	3.74	0.21
50%-RP/ $\text{SnS}_2$	40.96	3.76	0.23



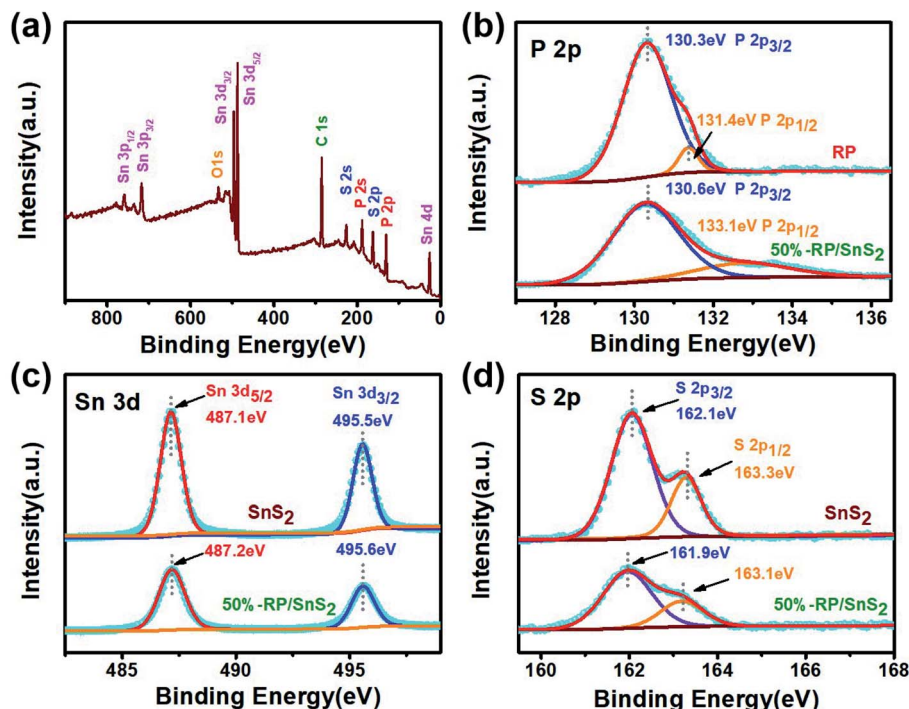


Fig. 5 (a) XPS survey spectra and corresponding high-resolution XPS spectra of (b) P 2p, (c) Sn 3d, (d) S 2p.

SnS<sub>2</sub> (Fig. 5(c)) displays two main peaks at 487.1 and 495.5 eV, assigned to Sn 3d<sub>5/2</sub> and 3d<sub>3/2</sub>, respectively.<sup>33,34</sup> The corresponding peak positions of RP/SnS<sub>2</sub> show minor shifts to 487.2 and 495.6 eV. Likewise, Fig. 5(d) suggests that the high-resolution S 2p spectrum for SnS<sub>2</sub> can be deconvoluted into two peaks at 162.1 and 163.3 eV, assigned to S 2p<sub>3/2</sub> and 2p<sub>1/2</sub>,<sup>35</sup> expressing minor shifts to lower binding energies 161.9 and 163.1 eV for RP/SnS<sub>2</sub>. As revealed from the mentioned results, the coupling between SnS<sub>2</sub> and RP altered the elemental binding energies for both of them, probably resulting from the electron transfer between semiconductors with different  $E_F$  levels.<sup>36</sup> This also indirectly implied that a nano-heterojunction was successfully established between SnS<sub>2</sub> and RP.

### 3.3 Photogenerated carrier transmission performance

As clearly identified from the above results, RP helps enhance the photocatalytic activity of SnS<sub>2</sub> by forming a nano-heterojunction. There into, the transmission mechanisms of carriers between semiconductors can be examined for an explanation. Photoluminescence (PL) spectra of SnS<sub>2</sub> and RP/SnS<sub>2</sub> under an excitation of 645 nm are presented to investigate the transfer behavior of photoinduced electrons and holes in photocatalysts. Fig. 6(a) suggests that the PL intensity of RP/SnS<sub>2</sub> was obviously lower than that of SnS<sub>2</sub>, demonstrating that the SnS<sub>2</sub> nanosheets with moderate amounts of RP can suppress the electron-hole recombination. To delve into the reason for the enhanced photocatalytic activity, time-resolved photoluminescence (TR-PL) spectra were collected (Fig. 6(b)) with radiative lifetimes ( $\tau_1$  and  $\tau_2$ ) and their corresponding coefficients ( $A_1$  and  $A_2$ ) in the inset of Fig. 6(b). Based on the

mentioned data, average fluorescence lifetimes ( $\tau$ ) can be obtained by the following formula,<sup>37</sup> *i.e.*, 0.69 ns and 0.73 ns for RP/SnS<sub>2</sub> and SnS<sub>2</sub>, respectively. The decreased average fluorescence lifetime means that the transfer of electrons between SnS<sub>2</sub> and RP was accelerated, which is conducive to facilitating photocatalytic reactions.

$$\tau = \frac{A_1\tau_1^2 + A_2\tau_2^2}{A_1\tau_1 + A_2\tau_2}$$

To further verify the role of RP in accelerating charge carrier separation, electrochemical measurements were performed, as shown in Fig. 7. It is known that the transient photocurrent response could manifest the separation and collection efficiency of hole-electron pairs occurring on the photocatalyst surface/interface.<sup>38</sup> Fig. 7(a) suggests that the number of photoinduced charge carriers generated under the light exposure of RP/SnS<sub>2</sub> was significantly higher than those of SnS<sub>2</sub> and RP (nearly 2–3 times), in agreement with the photocatalytic

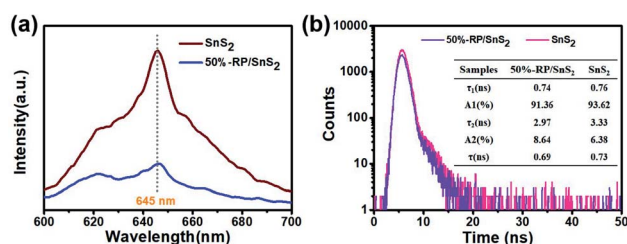


Fig. 6 (a) PL and (b) time-resolved fluorescence decay spectra and calculated average lifetime (inset) of samples.



Fig. 7 (a) Transient photocurrent response and (b) EIS spectra of the samples.

performance results reported above. Moreover, the radii of these samples identified in the Nyquist plots (Fig. 7(b)) complied with the sequence of RP/SnS<sub>2</sub> < SnS<sub>2</sub> < RP, revealing that RP/SnS<sub>2</sub> possessed the lowest resistance and fastest charge transfer kinetics for charge carriers.

### 3.4 Optical performance analysis

The optical properties are another vital factor in increasing the photoactivity and quantum yield. The enhanced light capture capacity of RP/SnS<sub>2</sub> was verified by UV-vis absorption spectroscopy. The tangent lines in the plots of the square root of the Kubelka–Munk functions against the photon energy were used to assess the band gaps ( $E_g$ ) of SnS<sub>2</sub> and RP. As displayed in Fig. 8(a) and (b), the absorption edge of SnS<sub>2</sub> was around 634 nm with a band gap of nearly 2.21 eV. However, RP exhibits a considerably strong absorption in the visible region, the absorption edge of which is at approximately 689 nm with a band gap of nearly 1.97 eV. An obvious absorption edge red-

shift could be identified in the RP/SnS<sub>2</sub> composites and the light absorption coefficient was integrally up-regulated in the 500–800 nm range. As revealed from the above results, the loading of RP nanosheets enhanced the optical properties of SnS<sub>2</sub>, thereby partially facilitating the enhancement of photocatalytic activity, in agreement with the previous results.

Moreover, Fig. 8(c) and (d) shows the XPS valence spectrum of SnS<sub>2</sub> and RP, in which the obtained valence band (VB) positions were identified as 1.53 eV and 1.83 eV, respectively. Meanwhile, the  $E_g$  measured *via* the optical absorption spectra above ( $E_g$  (SnS<sub>2</sub>) = 2.21 eV and  $E_g$  (RP) = 1.97 eV) indicates that the conduction band (CB) positions would respectively occur at about −0.44 eV and −0.38 eV for SnS<sub>2</sub> and RP. To identify the major active species accounting for organic pollutant degradation, disodium ethylenediaminetetraacetic acid (EDTA-Na<sub>2</sub>), benzoquinone (BQ), and isopropyl alcohol (IPA) solutions were respectively added to trap holes ( $h^+$ ), hydroxyl radicals ( $\cdot$ OH), and superoxide radicals ( $\cdot$ O<sub>2</sub><sup>−</sup>). According to Fig. 9, IPA slightly impacted the RhB degradation, demonstrating that  $\cdot$ OH are not the major reactive species in the photocatalytic oxidation process. However, upon the addition of EDTA-Na<sub>2</sub> and BQ, the efficiency decreased significantly, revealing that  $\cdot$ O<sub>2</sub><sup>−</sup> and  $h^+$  are the main reactive species in the photocatalytic oxidation. Moreover, as indicated by their relative positions and band structure,  $e^-$ ,  $h^+$  and  $\cdot$ O<sub>2</sub><sup>−</sup> are involved in the reactions theoretically.<sup>39,40</sup>

The reactive oxygen species was further detected by EPR for verification, in which DMPO was applied in aqueous and methanolic dispersions as a trapping reagent for the  $\cdot$ OH and  $\cdot$ O<sub>2</sub><sup>−</sup>. As expected, the signal of the DMPO- $\cdot$ OH was not found



Fig. 8 (a) UV-vis diffuse reflection spectra, (b) Kubelka–Munk plots converted from the UV-vis diffuse reflection spectra, valence band spectrum of (c) RP and (d) SnS<sub>2</sub>.





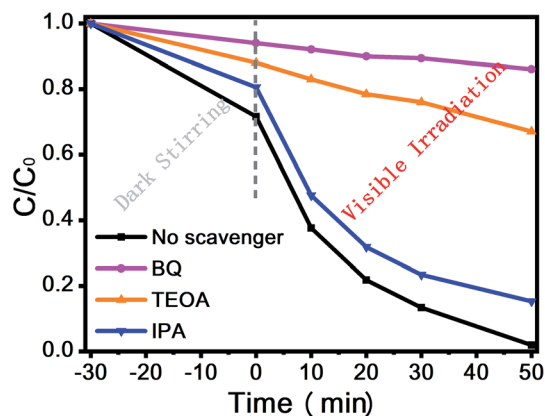


Fig. 9 Comparison of the effect of different quenchers on the photocatalytic reactions.



Fig. 10 EPR spectra of (a) DMPO-•OH in aqueous dispersion and (b) DMPO-O₂•⁻ in methanolic dispersion under light irradiation.

but the signal of the DMPO-O₂•⁻ was obvious, as shown in Fig. 10. These findings along with scavenger trapping experiments demonstrated that O₂•⁻ and h⁺ were the predominant active species in this photocatalytic reaction system.

As revealed from the analysis, the nano-heterojunction was built between SnS₂ and RP when the flower-like SnS₂ was modified by RP. The enhanced photocatalytic performance of RP/SnS₂ and photocatalytic synchronous removal of Cr(VI) and RhB was attributed to the critical role of nano RP. As described in Scheme 2, RP acts as the optical receiving active site to enhance the visible light response capability, thereby

generating and transmitting more electrons to the CB of SnS₂. Additionally, RP nanosheets created a proper transmission channel of carriers to inhibit the recombination of photo-generated holes and electrons. Furthermore, photogenerated electrons and the absorbed O₂ might be trapped on the SnS₂ surface to generate an abundant superoxide radical (O₂•⁻), thereby significantly impacting the photocatalytic degradation.

## 4. Conclusions

The proposed method for synchronous removal of Cr(VI) and RhB with RP/SnS₂ is promising based on the significantly increased degradation rate, expressing 8.2 and 10.8 times that of pristine SnS₂, as well as its high reusability. In the mentioned process, nano RP was introduced to act as an active site for both absorption enhancement and carrier separation with excellent dispersibility on the SnS₂ films. Moreover, the 2D heterojunction of the RP/SnS₂ photocatalyst created channels for the rapid transfer of photon-generated carriers; thus, photo-generated carriers can be effectively separated. Furthermore, the generation of abundant O₂•⁻ impacts the photocatalytic degradation oxidation reaction process. Overall, the application of RP/SnS₂ in the removal of coexisting Cr(VI)/RhB was demonstrated as a promising path toward treating wastewater.

## Conflicts of interest

There are no conflicts to declare.

## Acknowledgements

The present study was supported by the National Natural Science Foundation of China (Nos 21476183, 21676213, 21807087 and 21673173), the China Postdoctoral Science Foundation (No. 2016M600809), the Natural Science Basic Research Plan in Shaanxi Province of China (No. 2020JM422), Key Research and Development Program of Shaanxi (No. 2019KWZ-07), the Key Science and Technology Innovation Team of Shaanxi Province (No. 2017KCT-37), Technology Innovation Leading Program of Shaanxi (No. 2020TG-031) and the Xi'an City Science and Technology Project (No. 2019218214GXRC018CG019-GXYD18.4).

## References

- 1 R. Bruninghoff, A. Duijine, L. Braakhuis, P. Saha, A. Jeremiasse, B. Mei and G. Mul, Comparative Analysis of Photocatalytic and Electrochemical Degradation of 4-Ethylphenol in Saline Conditions, *Environ. Sci. Technol.*, 2019, 53, 8725–8735.
- 2 X. Liang, G. Wang, X. Dong, G. Wang, H. Ma and X. Zhang, Graphitic Carbon Nitride with Carbon Vacancies for Photocatalytic Degradation of Bisphenol A, *ACS Appl. Nano Mater.*, 2019, 2, 517–524.
- 3 S. Sharma, A. Umar, S. Mehta, A. Ibhaddon and S. Kansal, Solar light driven photocatalytic degradation of



Scheme 2 Schematic illustration of photocatalytic removal mechanism of Cr(VI) and organic pollutants over RP/SnS₂ composite.



- levofloxacin using  $\text{TiO}_2$ /carbon-dot nanocomposites, *New J. Chem.*, 2018, **42**, 7445–7456.
- 4 G. Fan, J. Zhan, J. Luo, J. Zhang, Z. Chen and Y. You, Photocatalytic degradation of naproxen by a  $\text{H}_2\text{O}_2$ -modified titanate nanomaterial under visible light irradiation, *Catal. Sci. Technol.*, 2019, **9**, 4614–4628.
  - 5 W. Liu, Y. Li, F. Liu, W. Jiang, D. Zhang and J. Liang, Visible-light-driven photocatalytic degradation of diclofenac by carbon quantum dots modified porous  $\text{g-C}_3\text{N}_4$ : Mechanisms, degradation pathway and DFT calculation, *Water Res.*, 2019, **151**, 8–19.
  - 6 S. Kampouri and K. Stylianou, Dual-Functional Photocatalysis for Simultaneous Hydrogen Production and Oxidation of Organic Substances, *ACS Catal.*, 2019, **9**, 4247–4270.
  - 7 P. Chen, L. Blaney, G. Cagnetta, J. Huang, B. Wang, Y. Wang, S. Deng and G. Yu, Degradation of Ofloxacin by Perylene Diimide Supramolecular Nanofiber Sunlight-Driven Photocatalysis, *Environ. Sci. Technol.*, 2019, **53**, 1564–1575.
  - 8 X. Liu, X. Chen, Y. Li, B. Wu, X. Luo, S. Ouyang, S. Luo, A. Kheraif and J. Lin, A  $\text{g-C}_3\text{N}_4$ @ $\text{Au@SrAl}_2\text{O}_4$ : $\text{Eu}^{2+}$ , $\text{Dy}^{3+}$  composite as an efficient plasmonic photocatalyst for round-the-clock environmental purification and hydrogen evolution, *J. Mater. Chem. A*, 2019, **7**, 19173–19186.
  - 9 J. Fu, Q. Xu, J. Low, C. Jiang and J. Yu, Ultrathin 2D/2D  $\text{WO}_3$ / $\text{g-C}_3\text{N}_4$  step scheme  $\text{H}_2$ -production photocatalyst, *Appl. Catal., B*, 2019, **243**, 556–565.
  - 10 F. He, A. Meng, B. Cheng, W. Ho and J. Yu, Enhanced photocatalytic  $\text{H}_2$ -production activity of  $\text{WO}_3/\text{TiO}_2$  step-scheme heterojunction by graphene modification, *Chin. J. Catal.*, 2020, **41**, 9–20.
  - 11 Q. Xu, L. Zhang, B. Cheng, J. Fan and J. Yu, S-Scheme Heterojunction Photocatalyst., *Chem*, 2020, **6**, 1543–1559.
  - 12 Q. Xu, L. Zhang, B. Cheng, J. Fan and J. Yu, S-Scheme Heterojunction Photocatalyst, *Chem*, 2020, **6**, 1543–1559.
  - 13 J. Yu, S. Wang, J. Low and W. Xiao, Enhanced photocatalytic performance of direct Z-scheme  $\text{g-C}_3\text{N}_4$ - $\text{TiO}_2$  photocatalysts for the decomposition of formaldehyde in air, *Phys. Chem. Chem. Phys.*, 2013, **15**, 16883–16890.
  - 14 I. Mondal, S. Moon, H. Lee, H. Kim and J. Park, Two-dimensional  $\text{FeS}_2$ -encapsulated Au: a quasi-epitaxial heterojunction for synergistic catalytic activity under photoelectrocatalytic water reduction, *J. Mater. Chem. A*, 2019, **7**, 19258–19268.
  - 15 C. Zhu, Y. Wang, Z. Jiang, F. Xu, Q. Xian, C. Sun, Q. Tong, W. Zou, X. Duan and S. Wang,  $\text{CeO}_2$  nanocrystal-modified layered  $\text{MoS}_2/\text{g-C}_3\text{N}_4$  as 0D/2D ternary composite for visible-light photocatalytic hydrogen evolution: Interfacial consecutive multi-step electron transfer and enhanced  $\text{H}_2\text{O}$  reactant adsorption, *Appl. Catal., B*, 2019, **259**, 118072.
  - 16 W. Chen, Z. He, G. Huang, C. Wu, W. Chen and X. Liu, Direct Z-scheme 2D/2D  $\text{MnIn}_2\text{S}_4/\text{g-C}_3\text{N}_4$  architectures with highly efficient photocatalytic activities towards treatment of pharmaceutical wastewater and hydrogen evolution, *Chem. Eng. J.*, 2019, **359**, 244–253.
  - 17 H. Wang, F. Liu, W. Fu, Z. Fang, W. Zhou and Z. Liu, Two-dimensional heterostructures: fabrication, characterization, and application, *Nanoscale*, 2014, **6**, 12250–12272.
  - 18 Y. Zhang, L. Yao, G. Zhang, D. Dionysiou, J. Li and X. Du, One-step hydrothermal synthesis of high-performance visible-light-driven  $\text{SnS}_2/\text{SnO}_2$  nanoheterojunction photocatalyst for the reduction of aqueous  $\text{Cr(IV)}$ , *Appl. Catal., B*, 2014, **144**, 730–738.
  - 19 X. Li, J. Zhu and H. Li, Comparative study on the mechanism in photocatalytic degradation of different-type organic dyes on  $\text{SnS}_2$  and  $\text{CdS}$ , *Appl. Catal., B*, 2012, **123–124**, 174–181.
  - 20 Y. Zhang, Z. Du, S. Li and M. Zhang, Novel synthesis and high visible light photocatalytic activity of  $\text{SnS}_2$  nanoflakes from  $\text{SnCl}_2 \cdot 2\text{H}_2\text{O}$  and S powders, *Appl. Catal., B*, 2010, **95**, 153–159.
  - 21 J. Pan, Z. Guan, J. Yang and Q. Li, Facile fabrication of  $\text{ZnIn}_2\text{S}_4/\text{SnS}_2$  3D heterostructure for efficient visible-light photocatalytic reduction of  $\text{Cr(VI)}$ , *Chin. J. Catal.*, 2020, **41**, 200–208.
  - 22 Y. Liu, D. Pan, M. Xiong, Y. Tao, X. Chen, D. Zhang, Y. Huang and G. Li, *In situ* fabrication  $\text{SnO}_2/\text{SnS}_2$  heterostructure for boosting the photocatalytic degradation of pollutants, *Chin. J. Catal.*, 2020, **41**, 1554–1563.
  - 23 D. Chen, S. Huang, R. Huang, Q. Zhang, T. T. Le, E. Cheng, R. Yue, Z. Hu and Z. Chen, Construction of Ni-doped  $\text{SnO}_2$ - $\text{SnS}_2$  heterojunctions with synergistic effect for enhanced photodegradation activity, *J. Hazard. Mater.*, 2019, **368**, 204–213.
  - 24 J. Zhang, G. Huang, J. Zeng, X. Jiang, Y. Shi, S. Lin, X. Chen, H. Wang, Z. Kong, J. Xi and Z. Ji,  $\text{SnS}_2$  nanosheets coupled with 2D ultrathin  $\text{MoS}_2$  nanolayers as face-to-face 2D/2D heterojunction photocatalysts with excellent photocatalytic and photoelectrochemical activities, *J. Alloys Compd.*, 2019, **775**, 726–735.
  - 25 X. Zhang, R. Zhang, S. Niu, J. Zheng and C. Guo, Construction of core-shell structured  $\text{WO}_3@/\text{SnS}_2$  heterojunction as a direct Z-scheme photo-catalyst, *J. Colloid Interface Sci.*, 2019, **554**, 229–238.
  - 26 L. Han, Y. Zhong, Y. Su, L. Wang, L. Zhu, X. Fei, Y. Dong, G. Hong, Y. Zhou and D. Fang, Nanocomposites based on 3D macroporous biomass carbon with  $\text{SnS}_2$  nanosheets hierarchical structure for efficient removal of hexavalent chromium, *Chem. Eng. J.*, 2019, **369**, 1138–1149.
  - 27 J. Xia, D. Zhu, L. Wang, B. Huang, X. Huang and X. M. Meng, Large-Scale Growth of Two-Dimensional  $\text{SnS}_2$  Crystals Driven by Screw Dislocations and Application to Photodetectors, *Adv. Funct. Mater.*, 2015, **25**, 4255–4261.
  - 28 Y. Sun, H. Cheng, S. Gao, Z. Sun, Q. Liu, Q. Liu, F. Lei, T. Yao, J. He, S. Wei and Y. Xie, Freestanding Tin Disulfide Single-Layers Realizing Efficient Visible Light Water Splitting, *Angew. Chem., Int. Ed.*, 2012, **51**, 8727–8731.
  - 29 J. Han, S. Lee and J. Cheon, Synthesis and structural transformations of colloidal 2D layered metal chalcogenide nanocrystals, *Chem. Soc. Rev.*, 2013, **42**, 2581–2591.
  - 30 S. Ansari, Z. Khan, M. Ansari and M. Cho, Earth-abundant stable elemental semiconductor red phosphorus-based hybrids for environmental remediation and energy storage applications, *RSC Adv.*, 2016, **6**, 44616–44629.





- 31 X. Bai, J. Wan, J. Jia, X. Hu, Y. He, C. He, E. Liu and J. Fan, Simultaneous photocatalytic removal of Cr(VI) and RhB over 2D MoS<sub>2</sub>/Red phosphorus heterostructure under visible light irradiation, *Mater. Lett.*, 2018, **222**, 187–191.
- 32 Y. Yan, M. Yang, H. Shi, C. Wang, J. Fan, E. Liu and X. Hu, CuInS<sub>2</sub> sensitized TiO<sub>2</sub> for enhanced photodegradation and hydrogen production, *Ceram. Int.*, 2019, **45**, 6093–6101.
- 33 Z. Zhang, C. Shao, X. Li, Y. Sun, M. Zhang, J. Mu, P. Zhang, Z. Guo and Y. Liu, Hierarchical assembly of ultrathin hexagonal SnS<sub>2</sub> nanosheets onto electrospun TiO<sub>2</sub> nanofibers: enhanced photocatalytic activity based on photoinduced interfacial charge transfer, *Nanoscale*, 2013, **5**, 606–618.
- 34 Y. Zhang, Z. Du, K. Li, M. Zhang and D. Dionysiou, High-Performance Visible-Light-Driven SnS<sub>2</sub>/SnO<sub>2</sub> Nanocomposite Photocatalyst Prepared via *In situ* Hydrothermal Oxidation of SnS<sub>2</sub> Nanoparticles, *ACS Appl. Mater. Interfaces*, 2011, **3**, 1528–1537.
- 35 J. F. Moulder, W. F. Stickle, P. E. Sobol and K. D. Bomben, Handbook of X-ray photoelectron spectroscopy: a reference book of standard spectra for identification and interpretation of XPS data, *Chem. Phys. Lett.*, 1963, **99**, 7–10.
- 36 M. Sun, J. Hu, C. Zhai, M. Zhu and J. Pan, CuI as hole-transport channel for enhancing photoelectrocatalytic activity by constructing CuI/BiOI heterojunction, *ACS Appl. Mater. Interfaces*, 2017, **9**, 13223–13230.
- 37 R. Shen, J. Xie, X. Lu, X. Chen and X. Li, Bifunctional Cu<sub>3</sub>P decorated g-C<sub>3</sub>N<sub>4</sub> nanosheets as a highly active and robust visible-light photocatalyst for H<sub>2</sub> production, *ACS Sustainable Chem. Eng.*, 2018, **6**, 4026–4036.
- 38 W. Xue, W. Chang, X. Hu, J. Fan, X. Bai and E. Liu, Highly dispersed copper cobalt oxide nanoclusters decorated carbon nitride with efficient heterogeneous interfaces for enhanced H<sub>2</sub> evolution, *J. Colloid Interface Sci.*, 2020, **576**, 203–216.
- 39 J. Kim, C. W. Lee and W. Choi, Platinized WO<sub>3</sub> as an environmental photocatalyst that generates OH radicals under visible light, *Environ. Sci. Technol.*, 2010, **44**, 6849–6854.
- 40 H. F. Cheng, B. B. Huang, Y. Dai, X. Y. Qin and X. Y. Zhang, One-step synthesis of the nanostructured AgI/BiOI composites with highly enhanced visible-light photocatalytic performances, *Langmuir*, 2010, **26**, 6618–6624.

